

# A breakage-based discrete element study of stress relaxation in quartz sands

Lei, Jiangtao; Arroyo, Marcos; Ciantia, Matteo; Zhang, Ningning

10.1007/s11440-025-02592-0

**Publication date** 

**Document Version** Final published version

Published in Acta Geotechnica

Citation (APA)

Lei, J., Arroyo, M., Ciantia, M., & Zhang, N. (2025). A breakage-based discrete element study of stress relaxation in quartz sands. Acta Geotechnica, 20(5), 2031-2048. Article 103230. https://doi.org/10.1007/s11440-025-02592-0

## Important note

To cite this publication, please use the final published version (if applicable). Please check the document version above.

Other than for strictly personal use, it is not permitted to download, forward or distribute the text or part of it, without the consent of the author(s) and/or copyright holder(s), unless the work is under an open content license such as Creative Commons.

Takedown policy

Please contact us and provide details if you believe this document breaches copyrights. We will remove access to the work immediately and investigate your claim.

## **RESEARCH PAPER**



# A breakage-based discrete element study of stress relaxation in quartz sands

Received: 19 August 2024 / Accepted: 18 February 2025 © The Author(s) 2025

#### **Abstract**

Stress relaxation of quartz sands is simulated using a recently proposed physically based time-to-fracture discrete element method framework. The framework incorporates time-dependency through stress-corrosion-induced grain fracture. This feature is embedded into a pre-existing particle-splitting-based rough-contact crushable model. The model is calibrated to represent Fontainebleau sand, a quartz sand. A controlled on-off computational strategy is adopted to advance the simulation efficiently. Model predictions are shown to compare favourably with laboratory results in oedometric and triaxial conditions in terms of stress relaxation and relaxation rate. Grain size distribution evolution is also tracked and shown to compare well with available laboratory results. The influence of initial mobilized strength  $q/q_{\rm max}$  on stress relaxation is recovered by the model, and explained through increased grain breakage. The simulated relaxation results are examined at the microscale and compared with those from creep experiments. The model displays the nonisochronous behaviour characteristic of sands. The relaxation tests display a state shift towards higher dilatancy conditions that may offer a possible explanation for some observations of pile set-up.

**Keywords** DEM · Particle crushing · Sand · Stress relaxation · Time dependence

## 1 Introduction

Several phenomena of large engineering significance cannot be properly understood without reference to time-dependent effects in granular soil, like creep—the accumulation of strain under constant effective stress—or stress relaxation—changes in stress without deformation. This is the case, for instance, of pile ageing (set-up): the remarkable shaft capacity increase with time that is

frequently observed on displacement piles in granular soils [28]. Delayed post-installation changes on the stress state around the pile, involving circumferential stress relaxation and radial stress increase along the pile shaft, have been frequently proposed as a plausible explanation for pile ageing [5, 14, 27, 29].

Stress relaxation like other macroscopic time-dependent effects observed in granular soils should result from microscale time-dependent phenomena. Laboratory evidence shows that the relaxation value at a specific time depends on the initial vertical stress, and after an elapsed time, the relaxed stress is roughly linear with respect to log-scale time (i.e. Lade and Karimpour [39]; Levin et al. [47]). Mitchell [52] examined possible microscale causes of time-dependent phenomena in granular soils and identified physical changes as generally more plausible than chemical or biological contributions. Physical changes involve changes in the size, shape or contact properties of grains from which granular fabric, strain and/or stress changes result. This hypothesis was given strong experimental support by the work of Lade and co-workers [30, 39, 40] who measured changes in grain size

Published online: 21 March 2025



<sup>☑</sup> Jiangtao Lei J.Lei@tudelft.nl

Division of Geotechnical Engineering and Geosciences, Department of Civil and Environmental Engineering, Polytechnic University of Catalonia (UPC), Barcelona, Spain

Offshore Engineering Section, Department of Hydrology, The faculty Civil Engineering & Geosciences, Delft University of Technology, Delft, Netherlands

<sup>&</sup>lt;sup>3</sup> School of Science and Engineering, University of Dundee, Dundee, UK

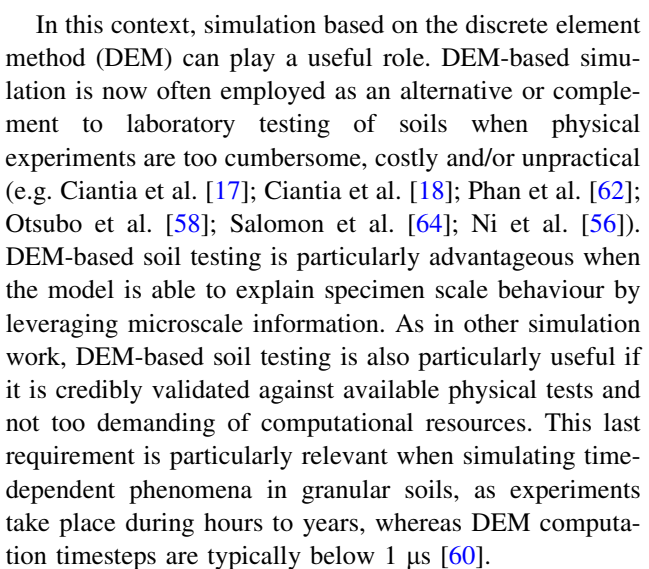
<sup>&</sup>lt;sup>4</sup> Università Degli Studi di Milano Bicocca, Milan, Italy

<sup>&</sup>lt;sup>5</sup> Ramboll, Hamburg, Germany

distribution (GSD) accompanying creep in several sands. The GSD changes observed were explained [38] as the result of delayed grain fracture or "static fatigue". This explanation fitted in nicely with separate research on rockfill materials, e.g. Oldecop and Alonso [57] illustrating the relevance of fracture growth on the time-dependent behaviour of those materials. Delayed granular fracture has been also incorporated into continuum constitutive models as a physically based alternative to more phenomenological visco-plastic models (e.g. Zhang and Buscarnera [73]).

In quartz sands granular fracture requires stress levels of the order of 5-10 MPa [38]. This contrasts with field measurements of radial stress on the shaft of displacement piles, which usually register low stress values (e.g. Lehane et al. [41], on the order of 50-100 kPa). However, more detailed calibration chamber tests measurements, reproduced by numerical simulation (e.g. Ciantia et al. [20], Zhang et al. [75]) indicate that radial stress levels up to a few MPa may be actually present around displacement piles. It is also clear, on the other hand, that the stress level induced below the tip of a displacement pile in sand is much higher than the radial stress acting on the shaft, attaining in jacked piles levels of the order of 10 MPa, similar to those registered by a CPT tip (e.g. Lehane et al. [41]). Measurements in driven piles are more difficult, but much higher stress levels have been reported (e.g. Kortsch and Krisch [32], indicate stress levels above 100 MPa during driven pile installation in sand). In summary, significant grain breakage is likely to take place around displacement piles.

The link between time-dependent phenomena and grain breakage in sands has been occasionally established through direct tomographic observation (Andò et al. [2]). However, in most cases, experimental support was obtained using post-mortem sieve analyses of test specimens [8, 12, 22, 25, 46, 65]. This kind of experiment is prone to errors [38]. In highly friable materials sieving itself may break particles. If breakage results mostly on fines these may agglomerate or adhere to larger particles. Indeed, sieve analyses after creep have failed to identify changes in GSD in several testing campaigns on granular soils (e.g. Lv et al. [50]; Levin et al. [48]). This suggests that other physical phenomena may be also involved in granular time-dependent phenomena. Changes in particle shape distributions have been documented alongside breakage during creep [25]. Time-dependent contact attrition has been identified in grain contact experiments [51] and, presumably, plays also a role in time-dependent phenomena at larger scales. It seems clear that unravelling the different contributions of varied microscale physical changes to time-dependent phenomena in granular soils would require costly, slow and generally demanding experimental work.



DEM studies of time-dependent phenomena on granular soils have followed different approaches. In some cases (Wang et al. [70]; Gao et al. [26]) phenomenological viscous models were directly introduced in interparticle contact laws. Such models produce results that are qualitatively similar to time-dependent phenomena observed in soils, but, if applied to a particular soil, they would need to be calibrated on specimen-scale response. These models are currently postulated to represent microscale phenomena other than particle breakage [24].

Viscous contact behaviour is also introduced in contact laws by means of rate process theory (RPT; Kuhn and Mitchell [33, 34]). Differently from phenomenological viscous models the formulation of contact rate-dependent behaviour in RPT aims to represent a particular physical mechanism: atomic-scale interactions at solid contacts (silica-silica bonds), activated through thermal energy (Kwok and Bolton [35]). RPT models produce results that are similar to time-dependent phenomena observed in soils. However, the viscous parameters predicted by RPT are scaled up by orders of magnitude to enable practical simulation. This scaling has a significant impact on the predicted model outcomes [49, 69] and, as a consequence, scaling factors are adjusted to match specimen scale responses. RPT models are currently postulated to represent phenomena other than particle breakage [49, 69, 72].

Particle breakage is instead central to another class of DEM models that aim to represent time-dependent phenomena in granular soils. Particle breakage is made time-dependent through static fatigue driven grain fracture. The particle breakage models that were initially proposed [36, 66, 71] employed bonded particle agglomerates to represent grains. Particle agglomerates are computationally expensive and severely limit the ability of such models to track GSD evolution. Also, because static fatigue takes place only at the intergranular bonds, calibration of



relevant parameters becomes highly reliant on specimen scale results [1, 71].

Recently Lei et al. [43] presented a new DEM methodology to simulate creep in granular soils that was also based on static fatigue driven grain fracture. Differently from previous efforts, this proposal does not use particle agglomerates and predicts GSD evolution with ease. Model calibration was also improved, using only information other than the specimen scale responses that the model was aiming to reproduce. Lei et al. [43] demonstrated the methodology showing its ability to reproduce creep experiments on quartz sands. In this work we examine the capabilities of this new methodology to reproduce another important time-dependent phenomenon: stress relaxation. One of the interesting aspects of this study is that even if we directly used the parameter fitted to creep simulation results, a good performance in stress relaxation can still be achieved. This is because the parameters we used are physically based and indicating the DEM model formulated here also has the potential to be extended to engineering scale directly, bypassing continuum models altogether. In what follows we briefly describe the model employed we then present the macroscopic results of relaxation test simulations, followed by some micromechanical inspection of the same. We conclude by comparing some aspects of creep and relaxation tests and discussing briefly the connections between the relaxation test results and pile set-up.

# 2 DEM model description

#### 2.1 Rough crushable contact model

Following Russell and Muir Wood [63], Ciantia et al. [16] proposed a particle breakage model for spherical elements based on the failure criterion combining both the characteristic limiting particle strength  $\sigma_{\rm lim}$  and the force contact area  $A_{\rm E}$ :

$$F_n \le \frac{\kappa}{f(\gamma, \nu)} \pi R^2 \sin^2 \theta = \sigma_{\lim} A_F \tag{1}$$

The formulation of  $\sigma_{\lim}$ , (Eq. (2)) introduced by Ciantia et al. [16, 19] includes a particle size effect as well as a random component of strength for particles of the same size. The latter effect indirectly represents the influence on breakage of aspects not directly included in the model, such as grain shape. $\theta$  is the solid angle 'seen' from the sphere centre.  $\frac{\kappa}{f(\chi,v)}$  given by Russell and Muir Wood [63]—represents the maximum tensile stress inside the particle and can be regarded as particle strength  $\sigma_{\lim}$ .  $\chi$  is a dimensionless shape parameter and represents the ratio between the characteristic uniaxial compressive and tensile

strength,  $\sigma^c$  and  $\sigma^t$  ( $\chi = \frac{|\sigma^c|}{\sigma^t} - 1$ ).  $\nu$  represents the Poisson's ratio

$$\sigma_{\lim} = \sigma_{\lim,0} \left(\frac{d}{d_0}\right)^{-\frac{3}{m_p}} \left(1 + X_{0,1} var\right) \tag{2}$$

where  $\sigma_{\lim,0}$  is the mean value of element strength at the reference diameter,  $d_0$ , d is the granular diameter,  $m_{\rm p}$  is a material parameter, var is the coefficient of variation of the sphere strength distribution with the diameter  $d_0$ , assumed normal.  $X_{0,1}$  is a random number sampled from the standard normal distribution.

Otsubo et al. [59] proposed a rough contact model, which incorporates the effect of particle surface roughness on contact stiffness into the regular Hertzian contact model. The rough contact model contains three successive regimes: asperity-dominated regime, transition regime, and Hertzian regime to better capture the effect of roughness on sand grain contact stiffness. Zhang et al. [74] incorporated this rough contact model into the particle failure model using the following relationship regarding contact area:

$$A_F = \pi R^2 \sin^2 \theta = \pi r_c \delta \tag{3}$$

where  $r_c = (\frac{1}{r_1} + \frac{1}{r_2})^{-1}$ ,  $r_1$  and  $r_2$  are radii of two contacting particles,  $\delta$  is contact overlap.

After substituting contact overlap  $\delta$  with contact normal force  $F_n$ , the particle failure criteria for the three successive regimes can be described as the following three equations:

In the asperity-dominated regime  $(F_n \le F_{nR1})$ :

$$F_{n} \leq \frac{1}{c} \sigma_{\lim} \pi r_{c} \left( \frac{F_{n}}{S_{q} E_{c} \sqrt{2 r_{c} S_{q}}} \right)$$

$$\left\{ \left[ \left( \frac{300 S_{q} E_{c} \sqrt{2 r_{c} S_{q}}}{4 E_{c} \sqrt{r_{c}}} \right)^{\frac{2}{3}} + n_{2} S_{q} \right] \frac{1}{100}^{\frac{1}{b}} + n_{1} S_{q} \right\}$$
(4)

In the transitional-dominated regime ( $F_{nR1} \le F_n < F_{nR2}$ ):

$$F_{n} \leq \sigma_{\lim} \pi r_{c} \left\{ \left[ \left( \frac{300 S_{q} E_{c} \sqrt{2 r_{c} S_{q}}}{4 E_{c} \sqrt{r_{c}}} \right)^{\frac{2}{3}} + n_{2} S_{q} \right]$$

$$\left( \frac{F_{n}}{100 S_{q} E_{c} \sqrt{2 r_{c} S_{q}}} \right)^{\frac{1}{b}} + n_{1} S_{q}$$

$$(5)$$

In the Hertzian regime  $(F_n \ge F_{nR2})$ :

$$F_{\rm n} \le \sigma_{\rm lim} \pi r_c \left[ \left( \frac{9F_{\rm n}^2}{16r_c E_c^2} \right)^{\frac{1}{3}} + n_1 S_q + n_2 S_q \right]$$
 (6)

where  $F_{nR1}$  and  $F_{nR2}$  are critical contact normal forces for three transitional regimes,  $E_c = \left(\frac{1-v_1^2}{E_1} + \frac{1-v_2^2}{E_2}\right)^{-1}$ ,  $E_1$ ,  $E_2$  are the Young's modulus of two contacting particles, respectively;  $v_1, v_2$  are their Poisson's ratios.  $S_q$  is the particle



roughness  $n_1$  and  $n_2$  are model parameters; b, c are constants to ensure stiffness continuity, which are functions of particle roughness  $S_q$  and the contact overlaps at the transitional contact normal force  $F_{nR1}$ ,  $F_{nR2}$ . Following [16] tangential contact stiffness  $k_s$  in our study is described by a simplified Hertz-Mindlin contact model. More details can be found in Zhang et al. [74]

Once the loading condition of one particle meets one of the failure conditions in Eq. (4) or (5) or (6), the particle will be substituted with 14 smaller particles following the splitting method introduced in Ciantia et al. [16]. Sibling particles are assigned particle strength ( $\sigma_{\rm lim}$ ) and initial crack half-length randomly. A numerical comminution limit  $d_{\rm c}$  is imposed to avoid crushing small particles and enhance computational efficiency. This requirement should be balanced with the fact that the value of the ratio  $d_{\rm c}/d_{50}$  does affect simulation outcomes and, if too large, would result in unrealistic macroscopic response. For Fontainebleau sand Ciantia et al. [71] present a sensitivity analysis indicating that good results were obtained using  $d_{\rm c}/d_{50} = 0.55$ .

Grading evolution may be quantified using the grading state index  $I_G$  [54], defined as the area ratio of current grading to a limit grading. The limit grading is calculated by the following equation with the fractal factor  $\gamma$ =2.6:

$$\frac{M_{(L< d)}}{M_{\rm T}} = \frac{d^{3-\gamma} - d_{\rm min}^{3-\gamma}}{d_{\rm max}^{3-\gamma} - d_{\rm min}^{3-\gamma}} \tag{7}$$

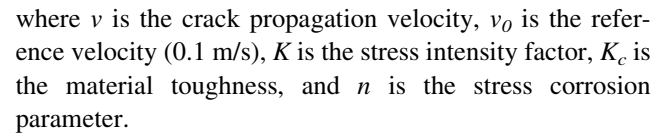
where  $M_{(L < d)}$  is the mass of particles whose diameter smaller than d;  $M_{\rm T}$  is the total mass.  $d_{max}$  and  $d_{min}$  are maximum and minimum diameter for the sample.

Some volume will be lost at each particle breakage with the replacement mechanism adopted in this study. The volume lost is assumed to correspond to fines and added to the grading evolution curve in post-processing. The GSD of lost mass at each particle breakage event is also estimated using Eq. (7), but with  $d_{\rm max}$  now representing the smallest particle generated during each crushing event. Previous studies (Ciantia et al. [15, 16, 18, 19]; Zhang et al. [74]) have shown that the overall mass lost using the propose method is small, and that increasing the number of sibling particles above 14 does not significantly affect macroscopic model results.

## 2.2 Time-dependent failure

Charles law [10] has been widely used to describe subcritical crack propagation under tensile loading, and it may be represented in normalized form [57] as:

$$v = v_0 \left(\frac{K}{K_c}\right)^n \tag{8}$$



The stress intensity factor K for tensile failure can be calculated in Eq. (9) according to Broek [7]:

$$K = \beta_c \sigma_I \sqrt{\pi a} \tag{9}$$

where  $\beta_c$  is the crack geometry parameter,  $\sigma_I$  is the far-field tensile stress, and a is the crack half-length.

Since  $K_c$  represents the stress intensity factor at the tensile strength limit  $\sigma_t$ , Eq. (10) can be obtained:

$$\frac{K}{K_c} = f_k \frac{\sigma_I}{\sigma_t} \tag{10}$$

where  $f_k$  is a geometry-dependent term, affected by specimen size and temperature.

In the Russell and Wood model [63], tensile strength  $\sigma_t$  and limit strength are directly proportional so  $\kappa = f(\chi, v)\sigma_{\text{lim}}$ ; on the other hand there is also a direct relation between maximum elastic tensile stress along the diameter beneath a contact force  $\sigma_t$  and the applied contact stress  $\sigma_{\text{mob}}$ ; Using those results Eq. (10) was rewritten in the following form by Lei et al.[43]:

$$\frac{K}{K_c} = f_k g(\chi, \nu) \frac{\sigma_{\text{mob}}}{\sigma_{\text{lim}}} \tag{11}$$

This equation is merely indicative, considering the uncertainty about crack distribution within the particle, particle shape, etc. Nevertheless, it does suggest that Charles law may be implemented in the DEM model simply through:

$$v = v_0 \left(\frac{\sigma_{\text{mob}}}{\sigma_{\text{lim}}}\right)^n \tag{12}$$

where v,  $v_0$ , and n are the same as those in Eq. (8),  $\sigma_{\rm mob}$  the mobilized maximum normal contact stress acting on a sphere, which can be obtained as the ratio of the contact normal force to the contact area ( $A_{\rm F}$  in Eq. 3).  $\sigma_{\rm lim}$  is the particle strength.

The crack half-length growth can be described by Eq. (13):

$$a = a_0 + v\Delta t \tag{13}$$

where  $a_0$  is the original crack half-length, randomly assigned to particles when they appear in the simulation. Crack lengths are sampled from a uniform distribution in the range of 0.001–0.5 d, where d is particle diameter. v is the crack propagation velocity, and  $\Delta t$  is the time interval for updating the crack. When the crack length grows to equal the particle diameter, 2a = d, the particle fails and is replaced using the same method as in the time-independent failure case.



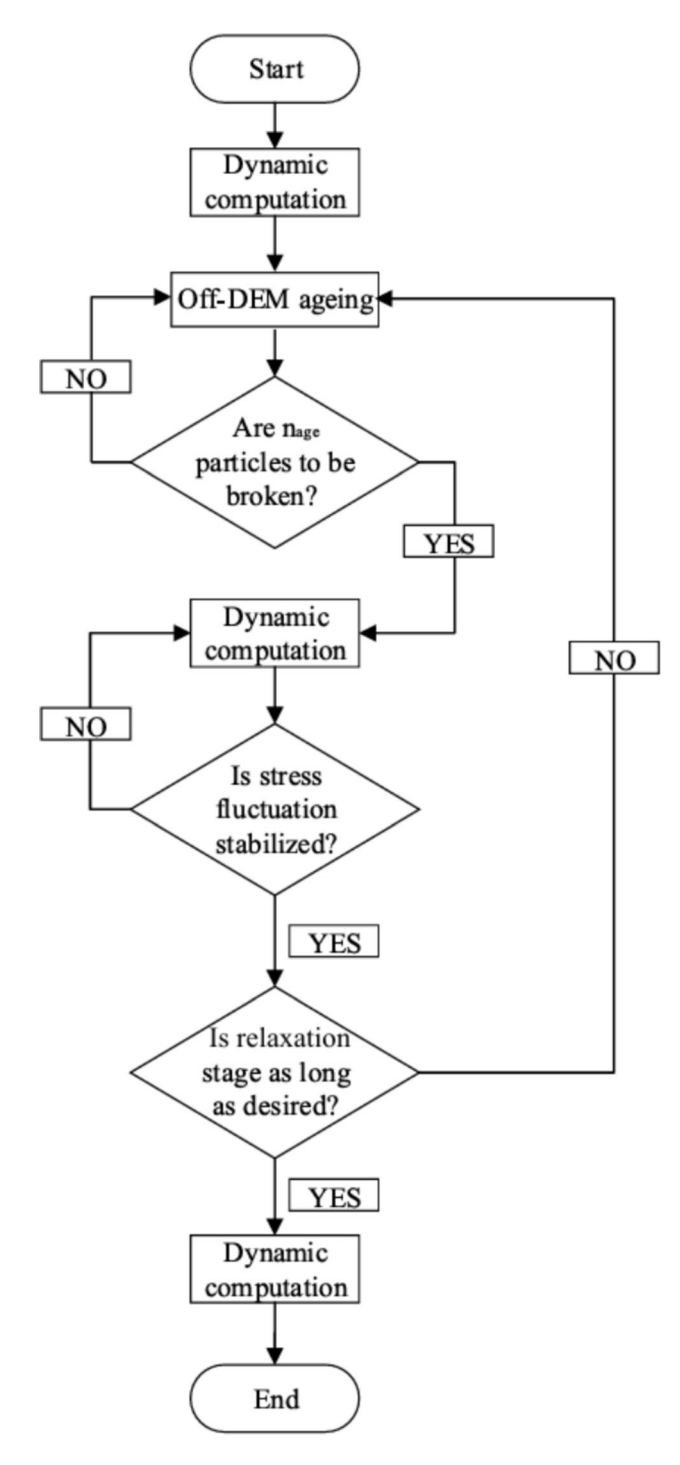


Fig. 1 Algorithm flow for Off-DEM ageing (adapted from Lei et al. [43])

## 2.3 Off-DEM ageing

Lei et al. [43] proposed an off-DEM ageing technique to advance time in creep simulation (Fig. 1). Similar on-off computation strategies have been applied in previous DEM simulation of time-dependent phenomena [68, 71]. This

technique was adapted in this study to simulate stress relaxation, as briefly described below.

The simulation alternates off-DEM ageing periods and periods of dynamic computation where DEM runs with all model features activated (wall and particle motion, contact stress updates, crack propagation, failure criterion checks, particle breaks etc.). During off-DEM ageing periods, only crack propagation is active, taking place at a constant velocity which is determined by maximum contact stress acting on the sphere at the end of previous dynamic computation period. Some particles fail as time advances during off-DEM ageing; those particles are counted until the number attains a certain limit value,  $(n_{age})$ . Then, the next dynamic computation stage is carried out, starting by simultaneous breakage all the  $n_{\rm age}$  particles. This simultaneous breakage sets up an oscillation around the imposed boundary condition that is dynamically tracked until the fluctuation stabilizes (Fig. 2). A minimum number of dynamic calculation cycles (150,000) is always applied. Lei et al. [44] carried out a series of sensitivity analysis to the effect of  $n_{age}$  on simulation results and no influence was shown when  $n_{\text{age}}$  was 30 or below. Simulations always start and end with a dynamic computation period.

#### 2.4 DEM model for Fontainebleau sand

For this study we have selected Fontainebleau sand as a representative quartz sand to calibrate the model on. Fontainebleau sand has been adopted as a prototype material in previous DEM simulations (Ciantia et al. [16]; [19]; Zhang et al. [74]).

The C++ plug-in option in PFC 3D (version 5.00.40) was used to implement the time-independent breakage model. Time-dependent breakage model and the off-DEM ageing technique were implemented through FISH, the high-level programming language of PFC.

Following Ciantia et al. [19], a cube of 4 mm side was employed as representative element volume (REV) for testing. The specimen is formed using radius expansion method (REM) with the target void ratio of 0.65 (corresponding to a relative density of 65% for the reference sand). The REM is a classical DEM initialization method, widely implemented in previous studies (e.g. Ciantia et al. [16, 19]; Bonneau et al. [6]; Chen and Martinez [11]; Chen et al. [13]; Dong et al. [23]). The test specimen is formed by randomly sampling the reference GSD distribution to generate particles in a cubical domain with reduced radius that are then expanded under isotropic stress condition until the target void ratio is attained. The final grain size distribution (GSD) of the REV closely matches that of Fontainebleau NE34 sand. The initial number of elements in the REV was 11,500.



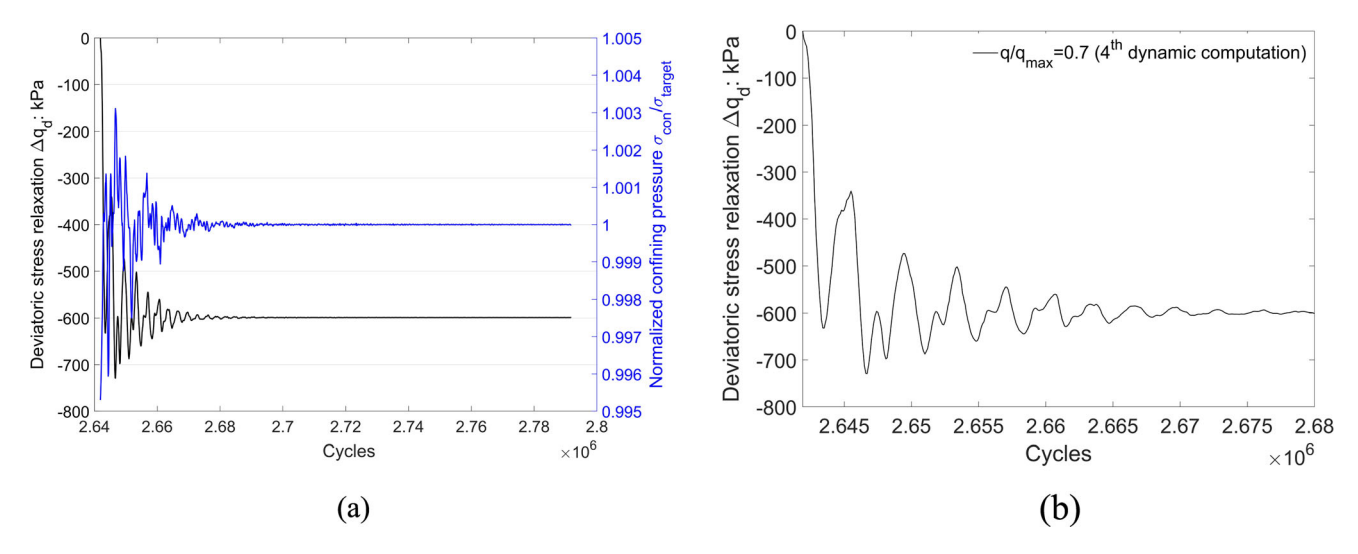


Fig. 2 Example of dynamic computation period during a triaxial drained stress relaxation test a Evolution of confining stress (blue) and deviatoric stress (black), b detail of the deviatoric stress drop (color figure online)

Table 1 Input parameters for time-to-fracture rough-crushable Fontainebleau sand model

GSD/mm			Basic contact model			Contact roughness			Instant failure criterion				Delayed failure	
$d_{50}$	$d_{max}$	$d_{min}$	G/GPa	ν	μ	$S_q/\mu m$	$n_1$	$n_2$	$m_{ m p}$	$\sigma_{lim,0}$ /GPa	var	$d_c / d_{50}$	$\overline{v_0}$	n
0.21	0.27	0.01	32	0.19	0.275	0.6	0.05	5	12	3.75	0.38	0.55	0.1 m/s	60

All elements employed are spherical. To roughly mimic particle shape effects, particle rotation was inhibited in all degrees of freedom. This is a simplification, dictated by computational efficiency, that has very little impact in macroscopic responses for quasi-static tests [3, 9, 67].

The parameters input to the model are collected in Table 1.

As indicated in the table there are five categories of input parameters:

a) Those that pertain to the grain size distribution (GSD) of the reference material (Fontainebleau sand). These are employed as such in the simulation, with no modification.

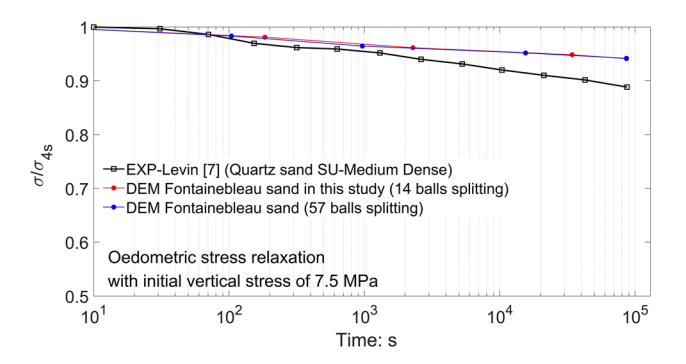


Fig. 3 Odeometric stress relaxation for calibrated Fontainebleau sand and experimental results for medium dense quartz sand (Levin [47])

b) Those that correspond to the basic Hertz-frictional contact model. The elastic parameters (G, ν) are directly obtained from quartz reference values, something that is made possible by the introduction of contact roughness (as explained by Zhang et al. [74]). Friction was calibrated to reproduce a triaxial

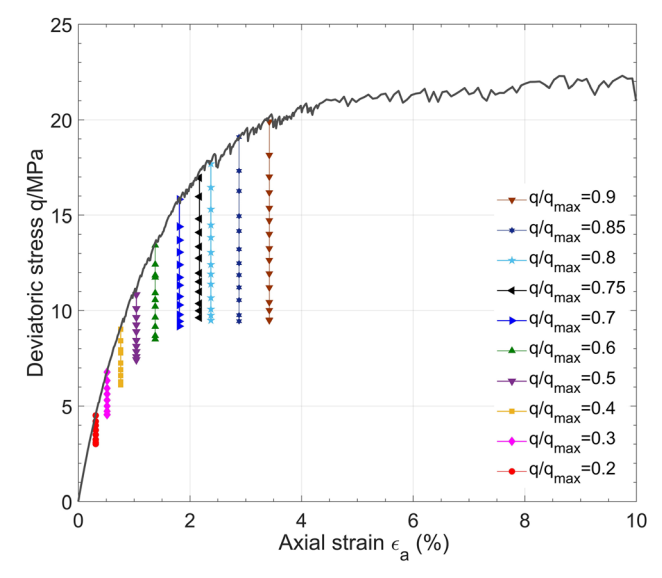


Fig. 4 Simulated monotonic triaxial shearing and stress relaxation



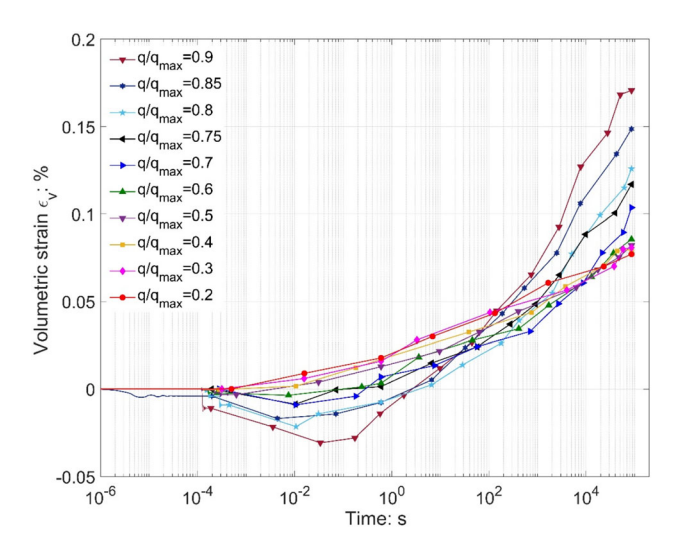


Fig. 5 Volumetric strain evolution during deviatoric stress relaxation tests

compression test on Fontainebleau sand (see Ciantia et al. [19])

- c) Parameters specific to the rough contact model were established in Zhang et al. [74]. Particle roughness *Sq* was determined considering particle roughness measurements on silica sand. The values of *n*1 and *n*2 were set by Zhang et al. [74] as 0.05 and 5, respectively, after calibrating the model against the results of single-particle contact experiments on a quartz sand (LBS; experiments reported by Nardelli and Coop [55]).
- d) Of the parameters corresponding to the instant failure criterion var,  $m_{\rm p}$  and  $\sigma_{lim,0}$  are obtained exploiting results of single-particle flat-platen crushing tests. The variance var is calibrated fitting a normal distribution to crushing strength data for particles of

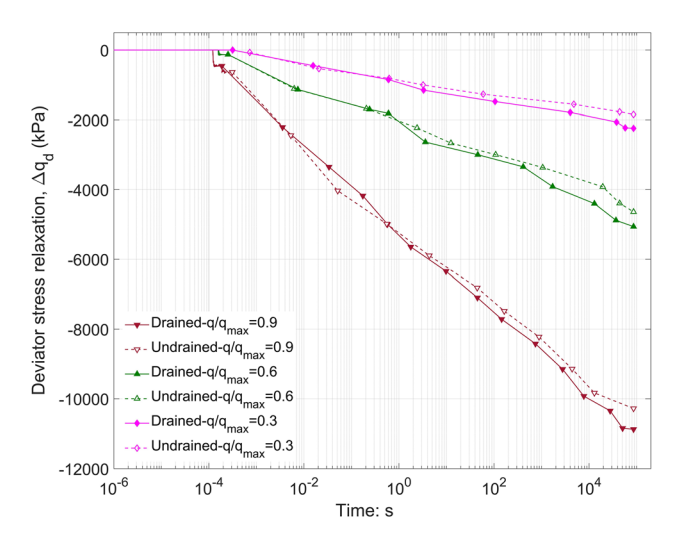


Fig. 6 Comparison of stress relaxation results under drained and undrained condition

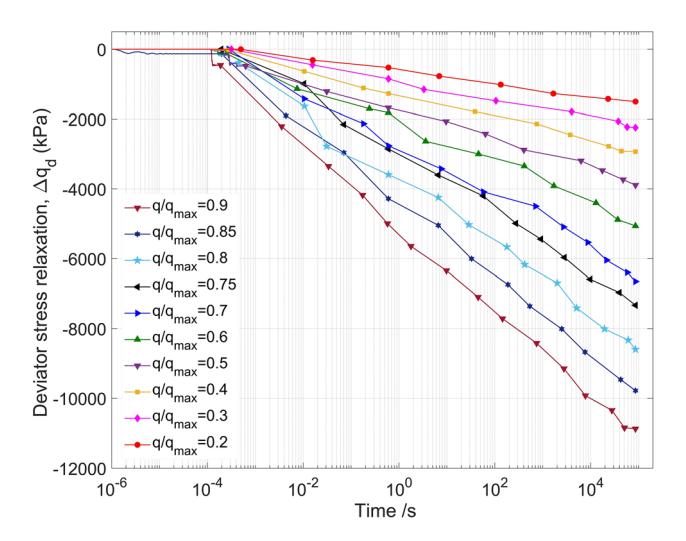


Fig. 7 Deviatoric stress relaxation evolution with time in DEM simulations

- a single size (Ciantia et al. [19]). The values of parameter  $m_{\rm p}$  and reference limit strength  $\sigma_{lim,0}$  are obtained fitting the size effect observed on mean values of particle crushing strength for a range of particle sizes (see Ciantia et al. [16, 19]). As noted above the limit comminution ratio  $d_{\rm c}/d_{50}$  was calibrated by Ciantia et al. [16] observing its effect on a high stress oedometric curve.
- e) Finally, the parameters controlling delayed particle failure were calibrated in Lei et al. [43] by reference to fracture data in the literature. Specifically, the reference velocity  $v_0$  was selected in line with fracture growth data reported by Oldecop and Alonso [57]. The stress corrosion index n was selected considering laboratory data of natural quartz and quartz-rich sandstone (see details in Lei et al. [43])

Lei et al. [43] verified that the model thus calibrated was able to reproduce the oedometer loading curve (void ratio vs vertical stress) and associated grading evolution observed in laboratory Fontainebleau NE34 sand tests [19].

#### 3 Macroscale observations

# 3.1 Oedometric stress relaxation

Levin [47] reports the results of an oedometric stress relaxation test on a quartz sand after applying an initial vertical stress of 7.5 MPa. A stress relaxation test under the same initial vertical stress was simulated using the calibrated parameters for Fontainebleau sand. The simulation was carried out with all walls fixed to ensure a zero-strain state. The simulation results are shown in Fig. 3. In the simulation curve, red dots correspond to the periods of



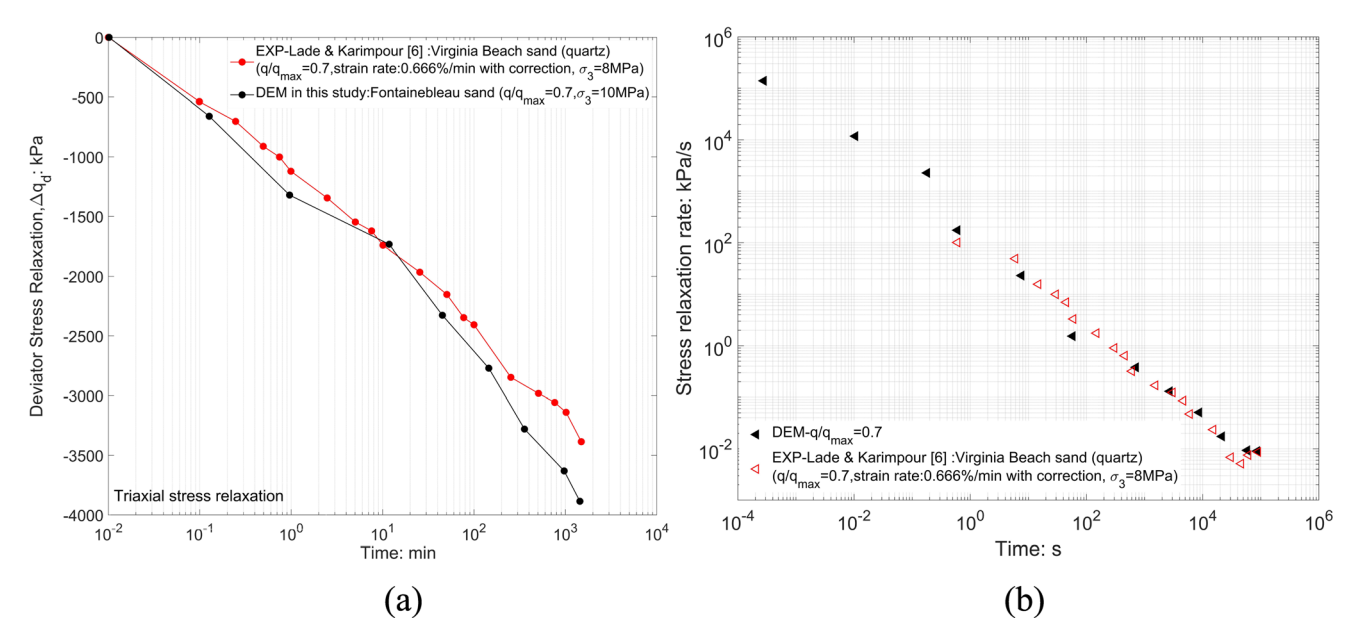


Fig. 8 DEM simulation for calibrated Fontainebleau sand and the laboratory results for Virginia beach sand (Lade and Karimpour [39]) a stress relaxation comparison, b relaxation rate comparison

dynamic computation, and the time between two red dots is the off-DEM ageing time. The value of stress relaxation is normalized by the value at 1 s. Considering that the model was not specifically re-calibrated for the quartz sand employed by Levin [47], an acceptable agreement can be observed between the simulation and the laboratory result. The oedometric test simulation was repeated to check the effect of lost mass upon particle breakage on stress relaxation. For this purpose, instead of the 14-particle splitting mechanism a 57-ball split, with lower mass loss [71] was employed. The results (Fig. 3) confirm the minimal effect of lost mass on stress relaxation.

## 3.2 Triaxial shear stress relaxation

Triaxial experiments of drained stress relaxation involve deviatoric stress relaxation under constant confining stress [37, 39, 61]. To conduct drained stress relaxation, the REV sample was first isotropically loaded up to a confining pressure of 10 MPa, a value selected to ensure significant particle breakage during shearing. Afterwards, a standard triaxial compression was conducted to identify the available shear strength. To this effect the specimen was sheared up to 30% deviatoric strain. Axial strain was imposed using a servo-controlled wall moving at 0.01 m/s, a velocity slow enough to ensure quasi-static conditions, with inertial number  $I < 2.68 \times 10^{-4}$ . The maximum mobilized strength of the REV corresponds to a deviatoric stress  $q_{\rm max}$  of 22.6 MPa (Fig. 4).

Drained stress relaxation tests were conducted starting at different deviatoric stresses corresponding to different levels of mobilized strength ( $q/q_{\rm max}$  values between 0.2, and 0.9). During relaxation tests the axial strain was maintained constant, fixing the top and bottom walls, while the servocontrol was active for the side walls to maintain the constant confining stress of 10 MPa. Each relaxation test lasted 1 day. Figure 4 shows the stress relaxation evolution of all cases. It can be seen that the amount of stress relaxation increases with the increase of mobilized strength. This was also observed by Lade and Karimpour [39] while conducting one-day stress relaxation tests on Virginia Beach sand. Relaxation magnitude increases with increased strength mobilization were also observed in simulations by Xu et al. [71] and Wang and Xia [69].

Although the axial strain was kept constant during the simulation, this was not the case for the radial strain, as the vertical walls were allowed to move to maintain a constant confining pressure. This made possible the apparition of small volumetric strains. Figure 5 shows the volumetric strain evolution during drained relaxation. The volumetric strains that accompany the one day drained relaxation tests remain below 0.18% for all cases. Lade and Karimpour [39] observed slightly smaller values (0.9–0.12%) of volumetric compression, which is reasonable considering that their relaxation experiments were conducted under a smaller confining pressure (8 MPa) than the one applied here. Xu et al. [71] also observed volumetric strains below 0.2% during simulation of drained relaxation.

To explore further the influence of volumetric strain during stress relaxation, three undrained relaxation tests, in which relaxation took place without any volumetric strain, were also carried out. This was achieved by fixing the 6



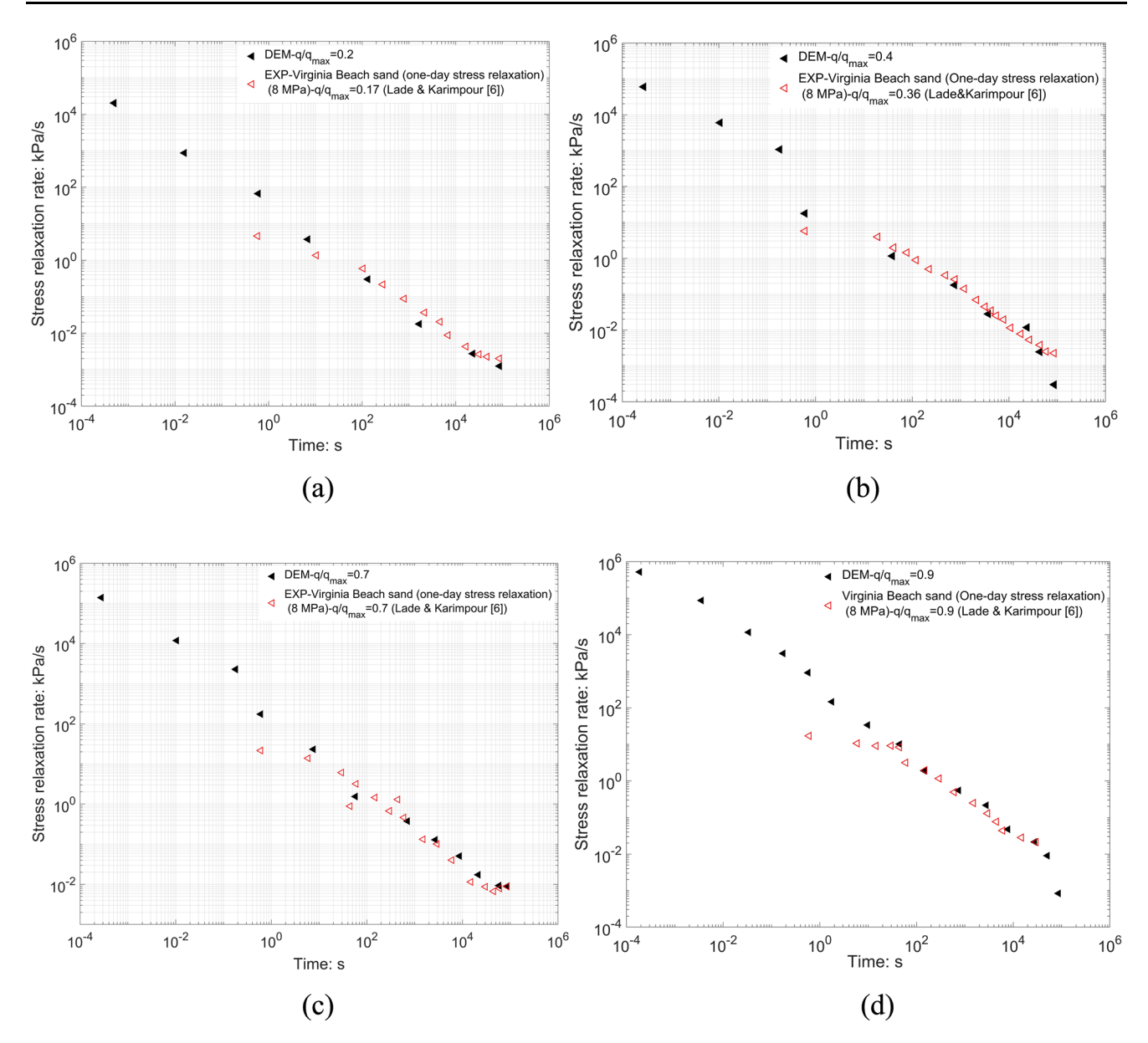


Fig. 9 Comparison of the axial strain rate evolution  $\mathbf{a} q/q_{\text{max}} = 0.2$ ,  $\mathbf{b} q/q_{\text{max}} = 0.4$ ,  $\mathbf{c} q/q_{\text{max}} = 0.7$ ,  $\mathbf{d} q/q_{\text{max}} = 0.9$ 

walls during the relaxation test. Test results are compared with results of drained relaxation in Fig. 6. Very similar relaxation trends can be observed. Undrained deviatoric stress relaxation is very similar—if slightly smaller—than drained deviatoric stress relaxation, and observation that was also made by Lade and Karimpour [39]. Since Fig. 6 indicates the similar stress relaxation results are obtained for the drained and undrained case, all the results presented afterwards are based on drained relaxation tests only.

Figure 7 shows the evolution of stress relaxation of all cases, it can be seen that relaxation trends to occur at a fixed rate and that such relaxation rate increases with the increase of  $q/q_{\rm max}$ . Figure 8 compares the deviatoric stress relaxation  $\Delta q_d$  and stress relaxation rate  $\dot{\Delta q}_d$  for the case q/q

 $q_{\rm max}=0.7$  obtained in the DEM simulation and in laboratory tests on Virginia Beach sand at the same relative stress level [39]. The comparison shows good agreement. The stress relaxation comparison uses as reference time for the start of relaxation 0.01 min, a value dictated by the time resolution that was attained in the laboratory experiments.

Lade and Karimpour [39] employed different triaxial shearing rates before their stress relaxation tests. They noted that the onset of relaxation was faster for tests sheared at a faster rate, but that the asymptotic relaxation rate attained was independent of the initial shearing rate. Their results in Fig. 8 correspond to the specimen sheared at the faster rate applied in the laboratory (0.666%/min),



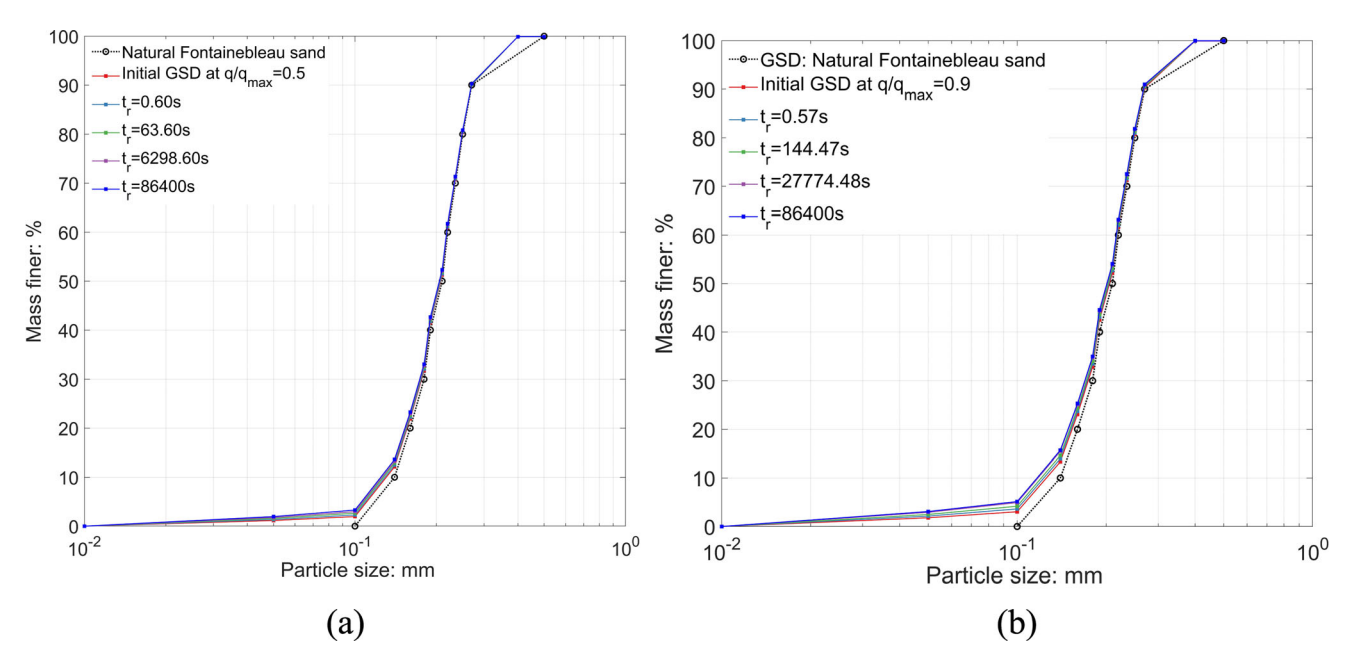


Fig. 10 GSD evolution during drained stress relaxation a  $q/q_{\rm max} = 0.5$ , b  $q/q_{\rm max} = 0.9$ 

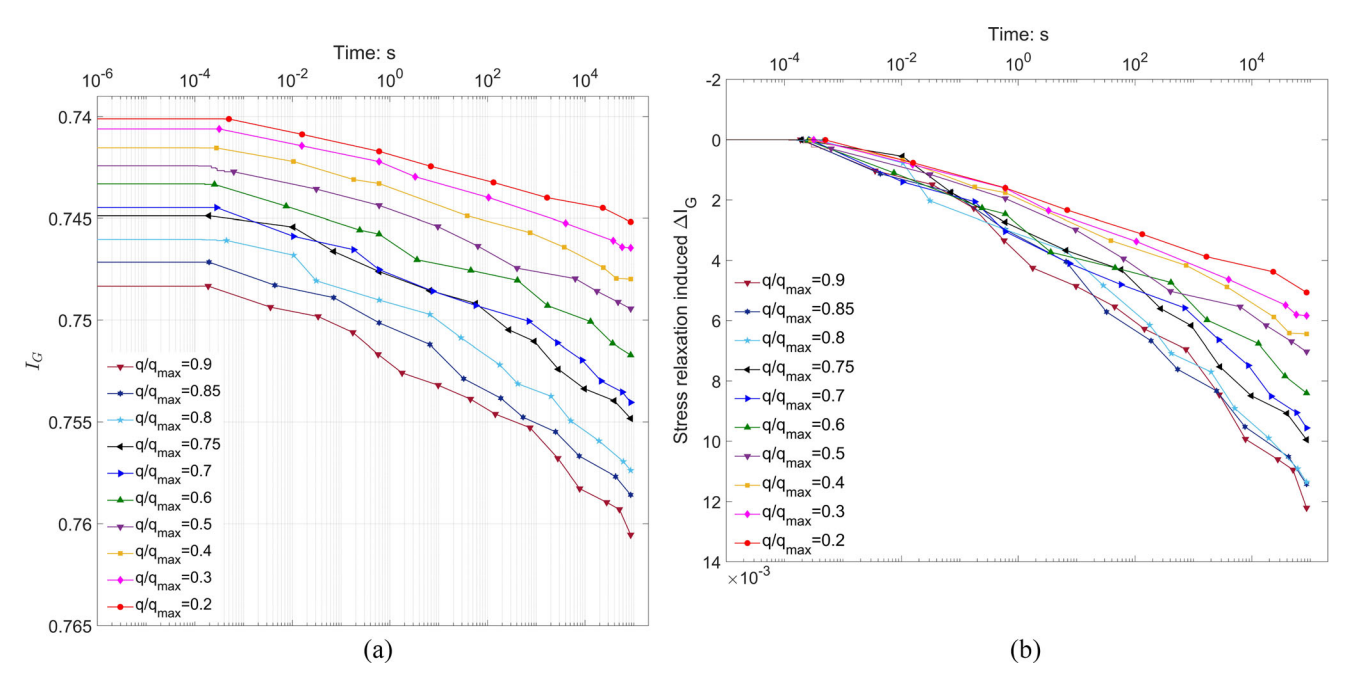


Fig. 11 Simulated Grading index evolution during stress relaxation a absolute values, b variation during relaxation phase

which showed immediate relaxation, with no delay. A more complete series of laboratory stress relaxation tests was available for specimens sheared at a lower rate (0.0416%/min). A comparison with the DEM results is presented in Fig. 9. The initial relaxation rates observed in the laboratory are slower but very good agreement is obtained in the asymptotic relaxation rates.

## 3.3 Triaxial shear stress relaxation: breakage

The simulations allow to track the evolution of GSD curves during stress relaxation, and results for  $q/q_{\rm max}=0.5$  and 0.9 are illustrated in Fig. 10. The GSD shifts are small for both tests, but it is nevertheless apparent that relaxation at  $q/q_{\rm max}=0.9$  was accompanied by more breakage than that at  $q/q_{\rm max}=0.5$ . The grading index  $I_{\rm G}$  evolution during stress relaxation is presented in more detail in Fig. 11.



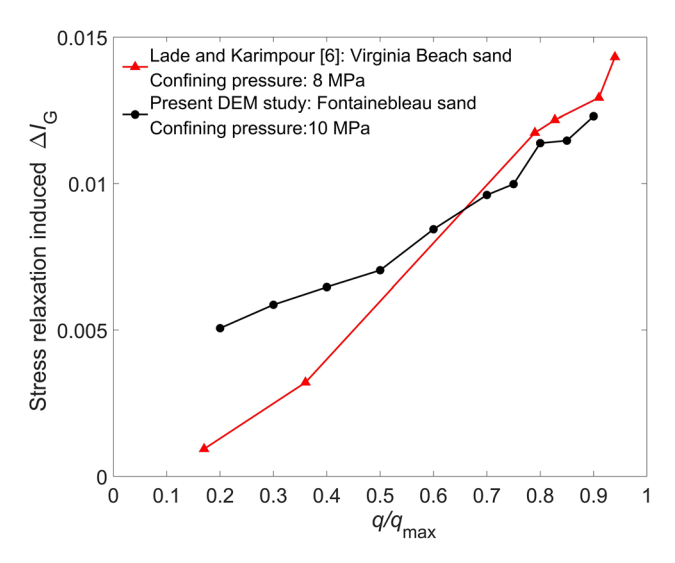


Fig. 12 One-day Stress relaxation induced change in breakage index  $I_{G}$  as a function of normalized initial shear strength

There is a clear trend for the grading index evolution rate to increase with the mobilized strength level at relaxation, a trend similar to that of the relaxation strain rate in Fig. 7.

It can be seen how the larger part of grading evolution takes place during shearing, with relaxation phases accruing only small changes in grading index, almost always less than  $10^{-2}$  (Fig. 11b). Measuring such small changes in grading in the laboratory is problematic, particularly as separation of the breakage accrued during shearing and that taking place during relaxation would require two different test specimens. These separate tests were not available to Lade and Karimpour [39], who, observing only the cumulative effect on grading of shearing and relaxation, concluded that breakage during relaxation was not significant and only "abrasion" was taking place. It is nevertheless possible to estimate the grading changes that took place during the relaxation phases of the laboratory tests on Virginia beach sand by Lade and Karimpour [39] using the information on breakage during continuous shearing of the

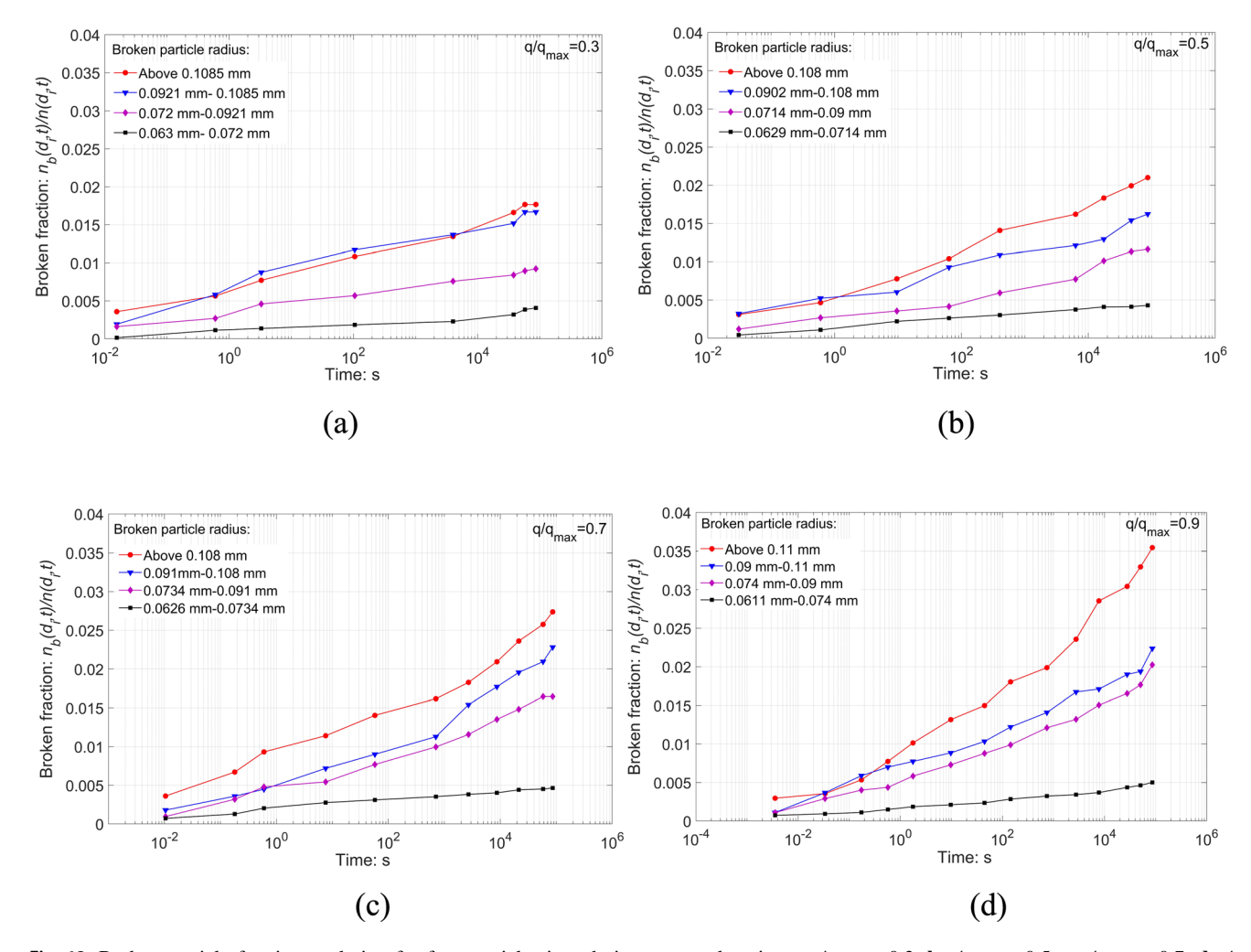


Fig. 13 Broken particle fraction evolution for four particle sizes during stress relaxation **a**  $q/q_{\text{max}} = 0.3$ , **b**  $q/q_{\text{max}} = 0.5$ , **c**  $q/q_{\text{max}} = 0.7$ , **d**  $q/q_{\text{max}} = 0.9$ 



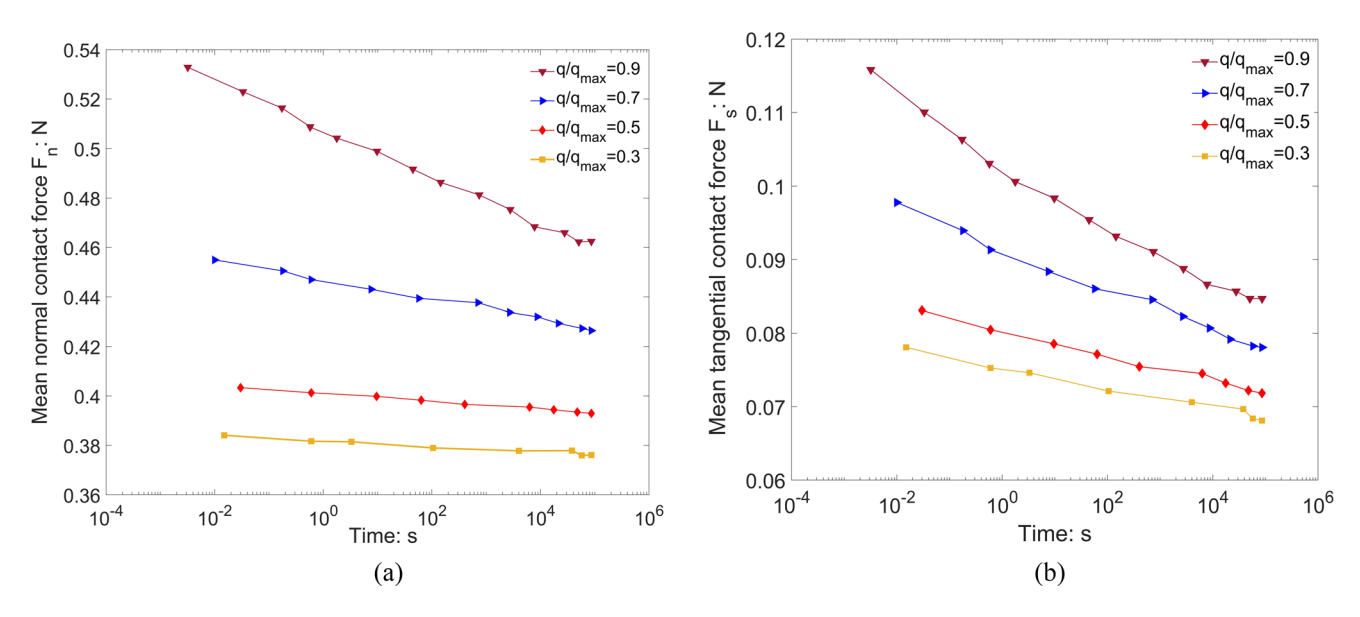


Fig. 14 Mean value evolution of a normal contact forces  $F_n$  and b tangential contact forces  $F_s$  in the REV cube during stress relaxation

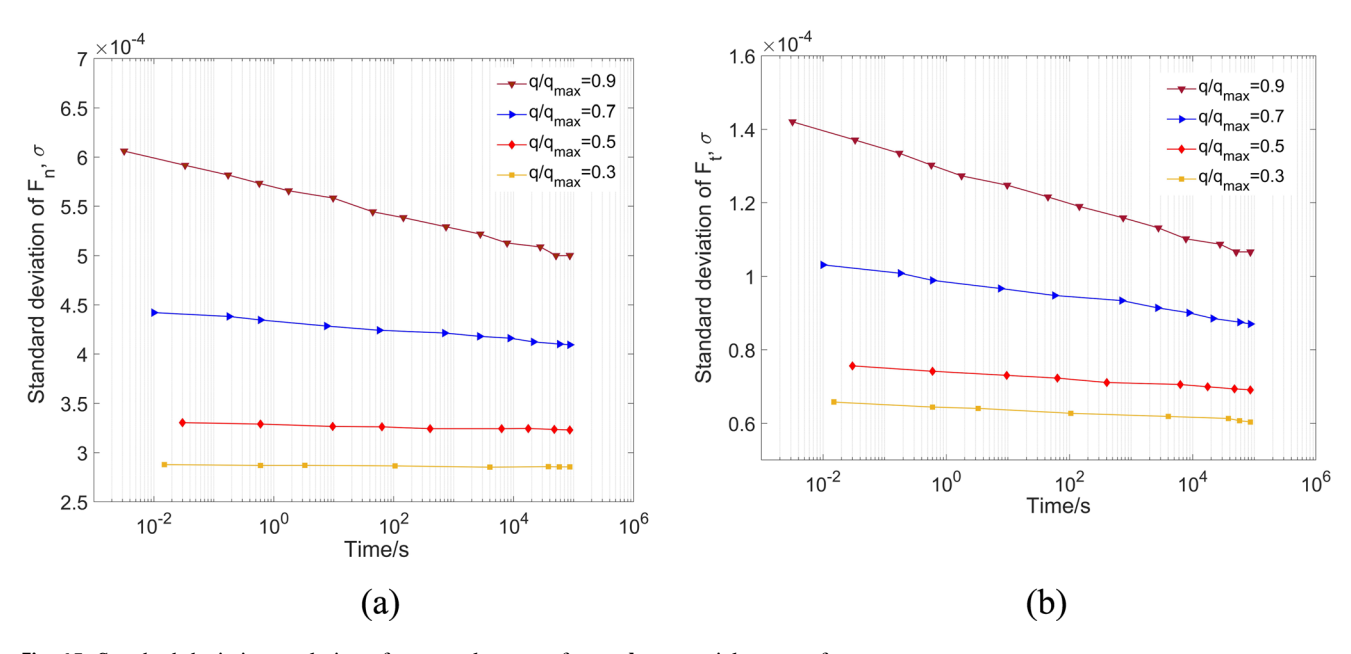


Fig. 15 Standard deviation evolution of a normal contact forces, b tangential contact forces

same sand presented graphically in Karimpour and Lade [30]. Doing so a comparison with the simulated results becomes possible and such comparison is presented in Fig. 12. The results from simulation are very similar to the laboratory ones, particularly for cases where  $q/q_{\rm max} > 0.5$ , where measurement and graph interpolation errors would be less significant.

## 4 Microscale observations

# 4.1 Breakage fraction

Once the link between particle breakage and stress relaxation has been established it is worth investigating it further at the particle scale. To this end we computed breakage fractions, defined as the accumulated number of particles  $d_i$  broken at time t divided by the initial number of particles of size  $d_i$ . The evolution of broken fractions for four particle sizes during stress relaxation tests is shown in Fig. 13. In all tests the larger particles are those that break more, as



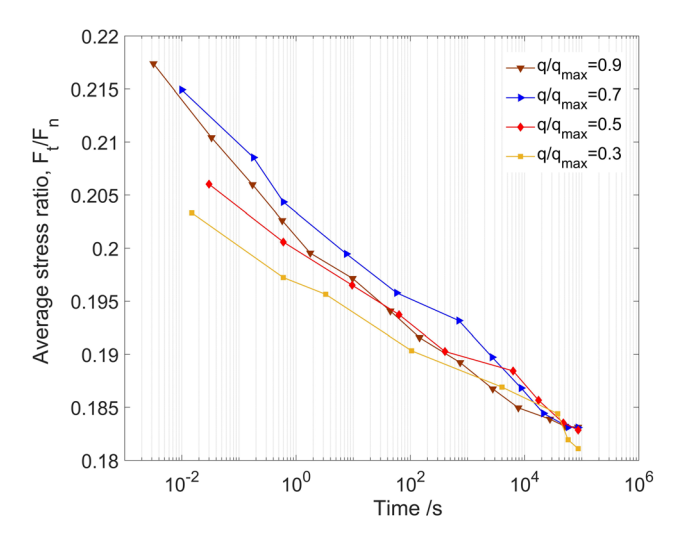
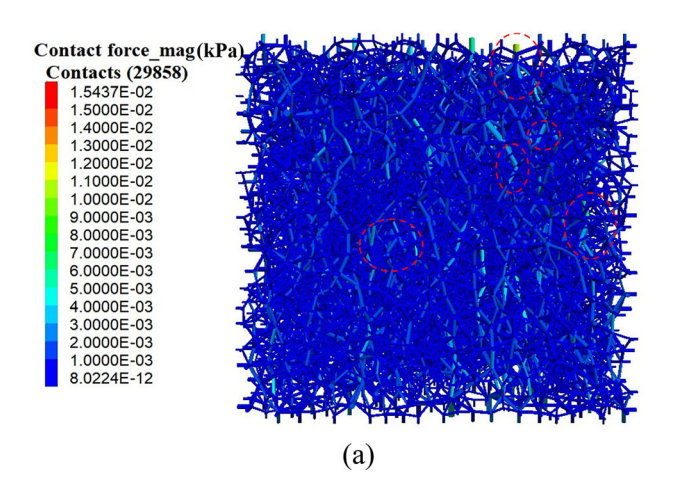


Fig. 16 Average stress ratio evolution during stress relaxation

expected given the size dependency law of particle strength. The difference between sizes increases with the increase of mobilized strength  $q/q_{\rm max}$ .

## 4.2 Force evolution during relaxation

Stress relaxation reflects relaxation taking place at the contact scale. Figure 14 shows the mean value evolution of contact normal forces and contact tangential forces during stress relaxation periods. A general decreasing trend can be observed for both components, with more pronounced decreases at higher initial shear mobilization rates. Contact forces also become slightly more homogenous during relaxation, and this applies again to both the normal and tangential components and, again, is more pronounced when relaxation takes place from a stress state closer to shear failure (Fig. 15). Similar observations were retrieved from RPT-based simulations by Wang and Xia [69].



Although both tangent and normal contact force components relax they do so at different rates, with tangent force relaxation happening at a faster rate. The net result is a decreasing contact force ratio. Figure 16 shows the evolution of average contact force ratio  $F_t/F_n$  during some relaxation cases. The decreasing of contact force ratio reflects how the specimen becomes more stable during stress relaxation, although the overall effects on the contact fabric are rather local. To further illustrate this, Fig. 17 shows representative contact force graphs for DEM samples relaxed from the highest mobilized strength  $(q/q_{\text{max}} = 0.9)$ . There are only a few strong force chains disappearing during relaxation, something that was also observed by Xu et al. [71] in their agglomerate-based simulations.

## 5 Discussion

# 5.1 Relaxation and creep

The final states of one-day stress relaxation in stress-strain plane can be connected together, to define a one-day relaxation curve. This curve may be compared with a one-day creep curve for the same test, obtained by extending the creep simulations presented by Lei et al. [43] to last one day. The results (Fig. 18) clearly show that the 24 h relaxation and creep curves obtained are different, with stress relaxation resulting in lower deviator stress at the same axial strain level. This behaviour was also found in Virginia Beach quartz sand by Lade and Karimpour [39] and, previously, in the more friable Antelope Valley sand [40]. This is described as non-isotach behaviour and is a distinctive feature of the time-dependent behaviour of granular soils (e.g. Augustesen et al. [4]). Non-isotach behaviour was also featured in the simulations presented by

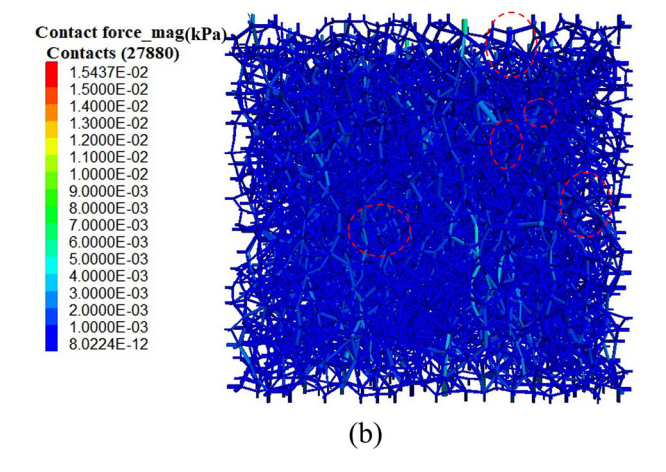


Fig. 17 Contact force contours of DEM samples with initial mobilized strength of  $q/q_{\text{max}} = 0.9$  a before stress relaxation, **b** after one-day stress relaxation



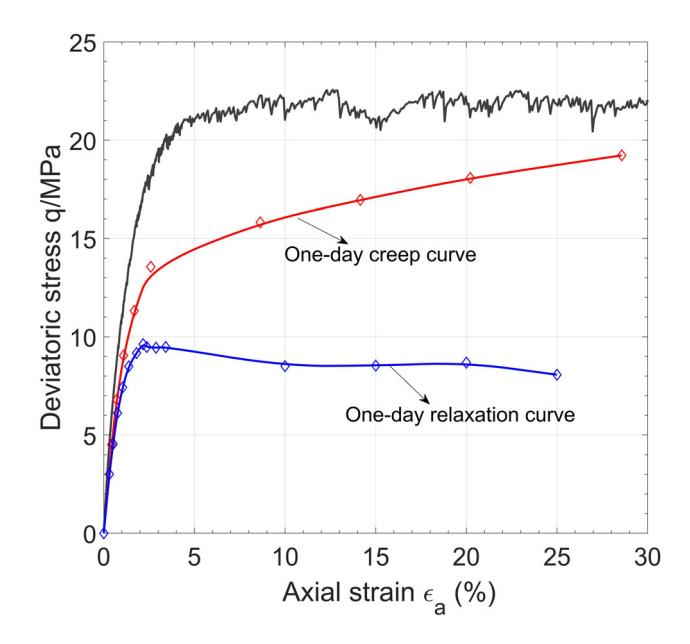
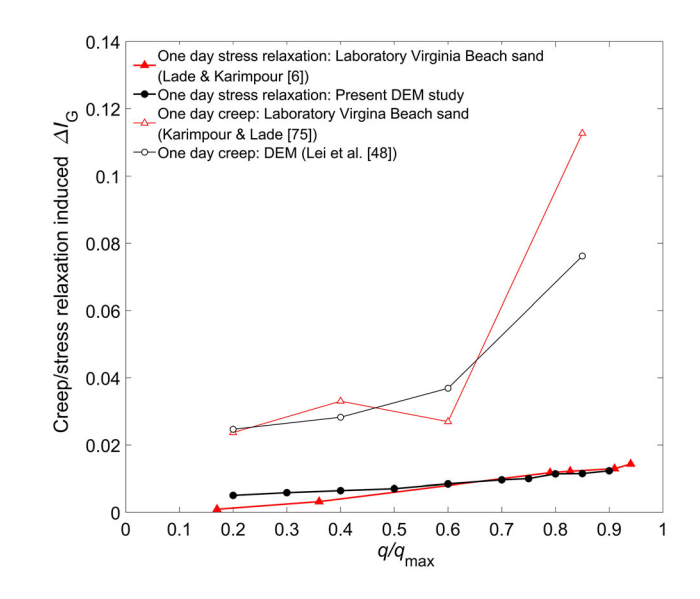


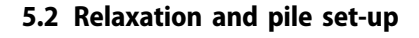
Fig. 18 One-day creep and one-day relaxation curve comparison



**Fig. 19** Change in grading index during one-day creep and relaxation phases

Xu et al. [71], based on time-dependent agglomerate bond degradation, as well as in those presented by Liu et al. [49] using the RPT model.

Starting from the same level of mobilized strength, creep is accompanied by much larger breakage than relaxation. Figure 19 presents grading index evolution from one day creep and relaxation phases as a function of initial mobilized strength: grading index evolution is much larger in the creep tests, reaching up to one order of magnitude at high mobilization rates.



In agreement with current methods of axial pile capacity evaluation pile set-up is conceptualized [14] as a post-in-stallation time-dependent change involving one or more of the following phenomena: radial effective stress increase around the pile, dilatancy increase around the pile or/and interface friction increase around the pile.

There is abundant experimental and numerical evidence indicating that particle crushing takes place during installation of piles on quartz sands and that crushed fragments cluster around the pile shaft [21]. The post-installation boundary condition along the pile shaft is likely a zero-strain one, similar to the boundary condition of stress relaxation tests. On this basis it is interesting to examine if the results presented above are able to shed some light on pile set-up, even if the relaxation time involved in the simulations (one day) is relatively small compared with those pertaining to pile set-up test observations.

In the context of pile set-up stress, stress relaxation is usually related to circumferential stress arching relaxation leading to radial stress increase [5, 14, 29]. This kind of mechanism needs to be investigated using the appropriate problem geometry, as arching around the pile would be directly related to pile radius. Therefore, the triaxial test results are not directly relevant for this purpose. It is nevertheless coherent with this hypothesis the fact that relaxation is more intense at higher mobilized stress ratios, as shown by Fig. 7. Stress mobilization is more intense around the pile tip [37] and measured radial stress increases after installation are also larger close to the pile tip [5, 27].

Consider now dilatancy increases, which have been also deduced from field pile tests results, (e.g. Axelsson [5]; Lehane et al. [42]; Gavin and Igoe [27]) perhaps even more consistently than radial stress increases, although the precise mechanisms involved in such increases are unclear. The relaxation test results shown above may be interpreted to suggest that a possible mechanism for that dilatancy increase may lie simply on the state changes induced by relaxation.

Lei et al. [45] obtained the critical state line (CSL) for the same rough-crushable DEM model of Fontainebleau sand using triaxial tests that involved no creep or relaxation phases. Following Ciantia et al. [19], triaxial critical states (constant void ratio and mobilized shear strength) were observed when the deviatoric strain of the sample reached 30%. The CSL thus obtained is represented (Fig. 20) in the e- $(p'/Pa)^{0.7}$  plane; where p' is the mean effective stress, and Pa is the atmospheric pressure. Figure 20 also represents the state shifts observed during the stress relaxation test phases. It can be seen that during relaxation states shift away from CSL after stress relaxation. All final states are



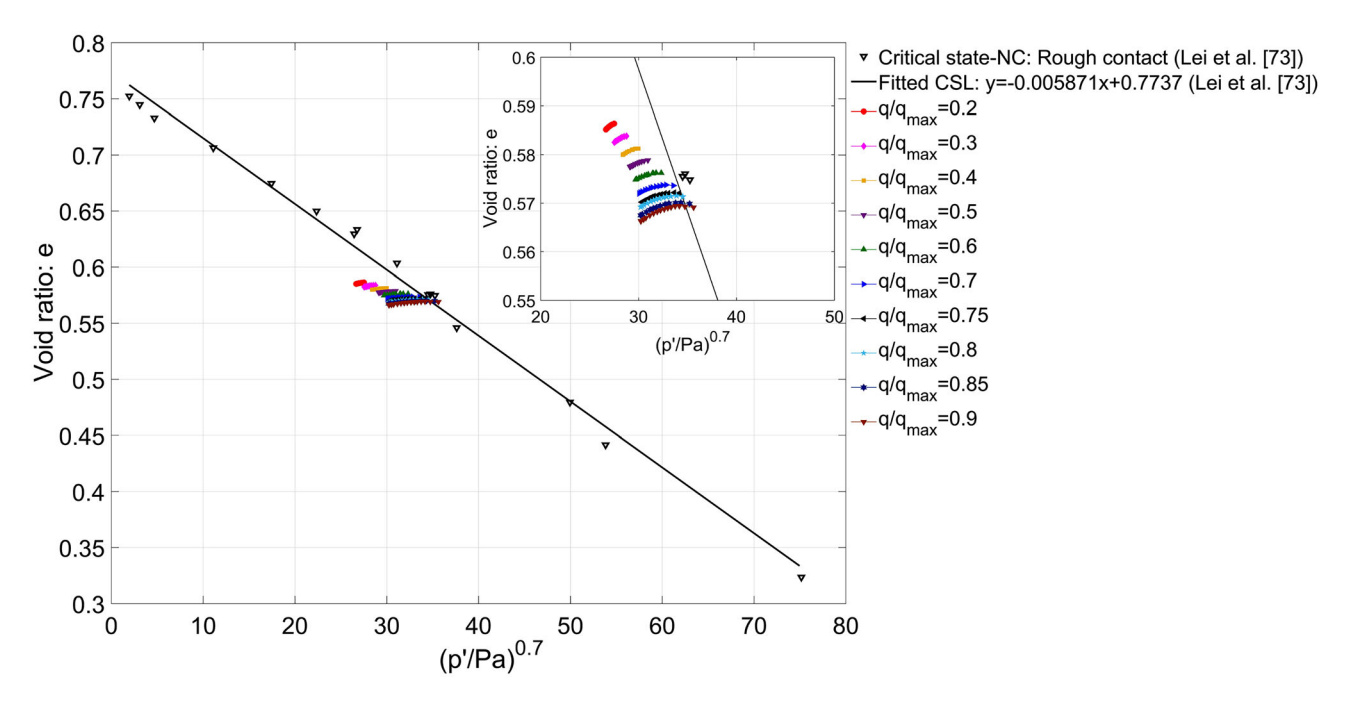


Fig. 20 State parameter shift of DEM Fontainebleau sand during drained stress relaxation

below the CSL, and therefore dilative, f the relaxed sand was sheared to reach critical state again, as it may happen during pile axial loading. The relaxation shifts are larger for the cases of high previous shear mobilization (0.85  $q_{\rm max}$  and 0.9  $q_{\rm max}$ ) in which the pre-relaxation state lies closer to the CSL. This is interesting, as critical state conditions are usually identified along the shaft upon simulations of continuous penetration tests (e.g. Monforte et al. [53]), which offer a good analogue for pile installation.

#### 6 Conclusions

This work set up to investigate the stress relaxation behaviour in sands at large stress using a new DEM simulation methodology based on static fatigue driven grain fracture. The reported simulation results compare well with the laboratory experiments of stress relaxation in terms of the amount of stress relaxation, stress relaxation rates, GSD evolution/particle breakage. Previous simulation work had not resulted in such wide agreement with independent laboratory experiment work. Some conclusions based on the work presented are:

- 1. The results of simulated stress relaxation tests compare favourably with available laboratory evidence in terms of stress relaxation magnitude and relaxation rate. The rate of relaxation increases with the increase of initial mobilized strength  $q/q_{\rm max}$ .
- 2. Particle breakage driven stress relaxation was made transparent by tracking the grading index  $I_G$  evolution.

- Simulated results compared well with available laboratory evidence.
- 3. The initial mobilized strength  $q/q_{\text{max}}$  increases the overall number of broken particles during stress relaxation, particularly for larger particle size.
- 4. Contact force homogenization takes place during stress relaxation, as revealed by a decreasing standard deviation of normal and tangential forces. The average contact force ratio  $F_t/F_n$  also decreases, indicates that the specimens became more stable during relaxation.
- When comparing creep and relaxation test results, the non-isotach behaviour characteristic of granular soils was recovered. It was also clear that creep is accompanied by much larger GSD evolution than relaxation.

The results mentioned above have some relevance for observations in pile set-up. Particle breakage driven stress relaxation may happen after pile installation and be, at least, partly responsible for increases in dilatancy around the pile shaft. This and other phenomena such as circumferential stress relaxation and associated radial stress increase may be further investigated using DEM models incorporating the methodology presented here.

**Acknowledgements** Spanish Research Agency support (AEI) through research project PID2020-119598RB-I00 is acknowledged.

Data availability Data will be made available on request.

## **Declarations**

Conflict of interest The authors declare no competing interests.



Open Access This article is licensed under a Creative Commons Attribution 4.0 International License, which permits use, sharing, adaptation, distribution and reproduction in any medium or format, as long as you give appropriate credit to the original author(s) and the source, provide a link to the Creative Commons licence, and indicate if changes were made. The images or other third party material in this article are included in the article's Creative Commons licence, unless indicated otherwise in a credit line to the material. If material is not included in the article's Creative Commons licence and your intended use is not permitted by statutory regulation or exceeds the permitted use, you will need to obtain permission directly from the copyright holder. To view a copy of this licence, visit http://creativecommons.org/licenses/by/4.0/.

## References

- Alonso EE, Tapias MA (2019) Suction and time effects in rockfill deformation. Int J Numer Analyt Methods Geomech 43(5):1032–1050. https://doi.org/10.1002/nag.2916
- 2. Andò E, Dijkstra J, Roubin E, Dano C, Boller E (2019) A peek into the origin of creep in sand. Granul Matter 21:1–8
- Arroyo M, Butlanska J, Gens A, Calvetti F, Jamiolkowski M (2011) Cone penetration tests in a virtual calibration chamber. Géotechnique 61(6):525–531. https://doi.org/10.1680/geot.9.P. 067
- Augustesen A, Liingaard M, Lade PV (2004) Evaluation of time dependent behavior of soils. Int J Geomech 4(3):137–156. https:// doi.org/10.1061/(ASCE)1532-3641(2004)4:3(137)
- Axelsson G (2000) Long-term set-up of driven piles in sand.
   Ph.D. thesis, Royal Institute of Technology, Stockholm, Sweden
- Bonneau F, Scholtes L, Rambure H (2021) An algorithm for generating mechanically sound sphere packings in geological models. Comput Part Mech 8:201–214
- Broek D (1986) Elementary engineering fracture mechanics. Martinus Nijhoff, Dordrecht
- Brzesowsky RH, Hangx SJT, Brantut N, Spiers CJ (2014) Compaction creep of sands due to time-dependent grain failure: effects of chemical environment, applied stress, and grain size. J Geophys Res Sol Earth 119(10):7521–7541. https://doi.org/10. 1002/2014JB011277
- Calvetti F (2008) Discrete modelling of granular materials and geotechnical problems. Eur J Environ Civ Eng 12(7–8):951–965
- Charles RJ (1958) Static fatigue of glass. J Appl Phys 29(11):1549–1560
- Chen Y, Martinez A (2023) DEM modeling of root circumnutation-inspired penetration in shallow granular materials. Géotechnique. https://doi.org/10.1680/jgeot.22.00258
- Chen X, Zhang J (2016) Effect of load duration on particle breakage and dilative behaviour of residual soil. J Geotech Geoenviron Engng 142(9):06016008
- Chen Y, Zhang N, Fuentes R, Martinez A (2023) A numerical study on the multi-cycle self burrowing of a dual-anchor probe in shallow coarse-grained soils of varying density. Acta Geotech. https://doi.org/10.1007/s11440-023-02088-9
- Chow FC, Jardine RJ, Brucey F, Nauroy JF (1998) Effects of time on capacity of pipe piles in dense marine sand. J Geotech Geoenviron Eng 124(3):254–264. https://doi.org/10.1061/ (ASCE)1090-0241(1998)124:3(254)
- Ciantia MO, Arroyo M, Butlanska J, Gens A (2016) DEM modelling of cone penetration tests in a double-porosity crushable granular material. Comput Geotech 73:109–127
- Ciantia MO, Arroyo M, Calvetti F, Gens A (2015) An approach to enhance efficiency of DEM modelling of soils with crushable

- grains. Géotechnique 65(2):91–110. https://doi.org/10.1680/geot. 13.P.218
- Ciantia MO, Arroyo M, Calvetti F, Gens A (2016) A numerical investigation of the incremental behavior of crushable granular soils. Int J Numer Analyt Methods Geomech 40(13):1773–1798
- Ciantia MO, Arroyo M, O'Sullivan C, Gens A (2019) Micromechanical inspection of incremental behaviour of crushable soils. Acta Geotech 14(5):1337–1356
- Ciantia MO, Arroyo M, O'Sullivan C, Gens A, Liu T (2019) Grading evolution and critical state in a discrete numerical model of Fontainebleau sand. Géotechnique 69(1):1–15. https://doi.org/ 10.1680/jgeot.17.P.023
- Ciantia M., O'sullivan, C., & Jardine, R. J. (2019). Pile penetration in crushable soils: Insights from micromechanical modelling. In 17th European Conference on soil Mechanics and Geotechnical Engineering (ECSMGE 2019). International Society for Soil Mechanics and Geotechnical Engineering.
- Ciantia MO, O'Sullivan C, Jardine RJ (2021) Installation effects on stress and grading around displacement piles in sand. In: Piling 2020: proceedings of the piling 2020 conference, ICE Publishing, pp 271–276
- Colliat-Dangus JL, Desrues J, Foray P (1988) Triaxial testing of granular soil underelevated cell pressure. In: Donaghe RT, Chaney RC, Silver ML (eds) Advanced triaxial testing of soil and rock. ASTM International, West Conshohocken, PA, USA, pp 290–310
- Dong Y, Fatahi B, Khabbaz H (2020) Three dimensional discrete element simulation of cylindrical cavity expansion from zero initial radius in sand. Comput Geotech 117:103230
- Gao Y, Chen Q, Yuan Q, Wang YH (2023) The kinematics and micro mechanism of creep in sand based on DEM simulations. Comput Geotech 153:105082
- Gao Y, Shi T, Yuan Q, Sun K (2024) The creep characteristics and related evolution of particle morphology for calcareous sand. Powder Technol 431:119077
- Gao Y, Wang YH, Su JC (2013) Mechanisms of aging-induced modulus changes in sand under isotropic and anisotropic loading. J Geotech Geoenviron Eng 139(3):470–482
- Gavin K, Igoe D (2021) A field investigation into the mechanisms of pile ageing in sand. Géotechnique 71(2):120–131. https://doi. org/10.1680/jgeot.18.P.235
- 28. Gavin KG, Jardine R, Karlsrud K, Lehane B (2015) The effects of pile ageing on the shaft capacity of offshore piles in sand. In Proc., Frontiers in Offshore Geotechnics III, 129–151. Taylor and Francis, Milton Park, UK
- Jardine RJ, Standing JR, Chow FC (2006) Some observations of the effects of time on the capacity of piles driven in sand. Géotechnique 56(4):227–244. https://doi.org/10.1680/geot.2006. 56.4.227
- Karimpour H, Lade PV (2010) Time Effects Relate to Crushing in Sand. J Geotech Geoenviron Eng 136(9):1209–1219. https:// doi.org/10.1061/(asce)gt.1943-5606.0000335
- Karimpour H, Lade PV (2013) Creep behavior in Virginia beach sand. Can Geotech J 50(11):1159–1178. https://doi.org/10.1139/ cgj-2012-0467
- 32. Kortsch, P., & Kirsch, F. (2022). Comparison of predicted and measured pile driving processes at steel pipe piles in North and Baltic Seas. 11th International Conference on Stress Wave Theory and Design and Testing Methods for Deep Foundations (SW2022), Rotterdam, The Netherlands. https://doi.org/10.5281/ zenodo.7148948
- Kuhn MR, Mitchell JK (1992) Modelling of soil creep with the discrete element method. Eng Comput 9(2):277–287. https://doi. org/10.1108/eb023866
- Kuhn MR, Mitchell JK (1993) New perspectives on soil creep ASCE. J Geotech Eng 119(3):507–524



- Kwok CY, Bolton MD (2010) DEM simulations of thermally activated creep in soils. Géotechnique 60(6):425–433. https://doi. org/10.1680/geot.2010.60.6.425
- Kwok CY, Bolton MD (2013) DEM simulations of soil creep due to particle crushing. Géotechnique 63(16):1365–1376
- Lacerda W, Houston WN (1973) Stress Relaxation in Soils. In: Proc. VIIIth. ICOSOMEF. Moscow 221–227
- 38. Lade PV, Karimpour H (2010) Static fatigue controls particle crushing and time effects in granular materials. Soils Found 50(5):573–583
- Lade PV, Karimpour H (2015) Stress relaxation behavior in Virginia Beach sand. Can Geotech J 52(7):813–835. https://doi. org/10.1139/cgj-2013-0463
- Lade PV, Nam J, Liggio CD (2010) Effects of particle crushing in stress drop-relaxation experiments on crushed coral sand.
   J Geotech Geoenviron Eng 136(3):500–509. https://doi.org/10. 1061/(asce)gt.1943-5606.0000212
- Lehane BM, Jardine RJ, Bond AJ, Frank R (1993) Mechanisms of shaft friction in sand from instrumented pile tests. J Geotech Eng 119(1):19–35
- Lehane BM, Schneider JA, Lim JK, Mortara G (2012) Shaft friction from instrumented displacement piles in an uncemented calcareous sand. J Geotech Geoenviron Eng 138(11):1357–1368
- Lei J, Arroyo M, Ciantia MO, Zhang N (2025) A fracture-based discrete model for simulating creep in quartz sands. Géotechnique 75(3): 393–407. https://doi.org/10.1680/jgeot.23.00068
- 44. Lei J, Arroyo M, Ciantia M, Zhang N (2023) A time-to fracture DEM model for simulating creep in rough crushable sand. In Proceedings of 10th European conference on numerical methods in geotechnical engineering, London, UK https://doi.org/10. 53243/NUMGE2023-37
- 45. Lei J, Arroyo M, Ciantia M, Zhang N (2021) Grain roughness effect on the critical state line of crushable sands. In: Proceedings of the 18th UK Travelling Workshop: GeoMechanics: from Micro to Macro (GM3), Dundee. https://doi.org/10.20933/ 100001234
- Leung CF, Lee FH, Yet NS (1997) The role of particle breakage in pile creep in sand. Can Geotech J 33(6):888–898
- Levin F (2021) Time-dependent compression behavior of sands under oedometric conditions. J Geotech Geoenviron Eng 147(12):04021144. https://doi.org/10.1061/(asce)gt.1943-5606. 0002664
- Levin F, Vogt S, Cudmani R (2019) Time-dependent behaviour of sand with different fine contents under oedometric loading. Can Geotech J 56(1):102–115. https://doi.org/10.1139/cgj-2017-0565
- Liu S, Wang J, Kwok CY (2019) DEM simulation of creep in one-dimensional compression of crushable sand. J Geotech Geoenviron Eng. https://doi.org/10.1061/(asce)gt.1943-5606. 0002098
- Lv Y, Li F, Liu Y, Fan P, Wang M (2017) Comparative study of coral sand and silica sand in creep under general stress states. Can Geotech J 54(11):1601–1611
- Michalowski RL, Wang Z, Nadukuru SS (2018) Maturing of contacts and ageing of silica sand. Géotechnique 68(2):133–145. https://doi.org/10.1680/jgeot.16.P.321
- Mitchell JK (2008) Aging of sand-a continuing enigma? Proceedings of the 6th international conference on case histories in geotechnical engineering, Missouri University of Science and Technology (2008), USA
- Monforte L, Gen A, Arroyo M, Mánica M, Carbonell JM (2021) Analysis of cone penetration in brittle liquefiable soils. Comput Geotech 134:104123
- Muir Wood D (2007) The magic of sands—the 20th Bjerrum Lecture presented in Oslo, 25 November 2005. Can Geotech J 44(11):1329–1350

- Nardelli V, Coop MR (2019) The experimental contact behaviour of natural sands: normal and tangential loading. Géotechnique 69(8):672–686. https://doi.org/10.1680/jgeot.17.P.167
- Ni X, Ma J, Zhang F (2024) Mechanism of the variation in axial strain of sand subjected to undrained cyclic triaxial loading explained by DEM with non-spherical particles. Comput Geotech 165:105846
- Oldecop L, Alonso E (2007) Theoretical investigation of the time-dependent behaviour of rockfill. Géotechnique 57(3):289–301. https://doi.org/10.1680/geot.2007.57.3.289
- Otsubo M, Chitravel S, Kuwano R, Hanley KJ, Kyokawa H, Koseki J (2022) Linking inherent anisotropy with liquefaction phenomena of granular materials by means of DEM analysis. Soils Found 62(5):101202
- Otsubo M, O'Sullivan C, Hanley KJ, Sim WW (2017) The influence of particle surface roughness on elastic stiffness and dynamic response. Géotechnique 67(5):452–459. https://doi.org/ 10.1680/jgeot.16.P.050
- Otsubo M, O'Sullivan C, Shire T (2017) Empirical assess ment of the critical time increment in explicit particulate discrete element method simulations. Comput Geotech 86:67–79
- Pham Van Bang D, di Benedetto H, Duttine A, Ezaoui A (2007)
   Viscous behaviour of dry sand. Int J Numer Analyt Methods Geomech 31(15):1631–1658. https://doi.org/10.1002/nag.606
- Phan QT, Bui HH, Nguyen GD, Bouazza A (2021) Effect of particle rolling resistance on drained and undrained behaviour of silty sand. Acta Geotech 16:2657–2682
- Russell AR, Muir Wood D (2009) Point load tests and strength measurements for brittle spheres. Int J Rock Mech Min Sci 46(2):272–280. https://doi.org/10.1016/j.ijrmms.2008.04.004
- Salomon J, Morimoto T, Patino-Ramirez F, O'Sullivan C (2024)
   Quantifying shear-induced permeability changes in mediumloose sands. J Geotech Geoenviron Eng 150(2):04023133
- Takei M, Kusakabe O, Hayashi T (2001) Time-dependent behavior of crushable materials in one-dimensional compression tests. Soils Found 41(1):97–121. https://doi.org/10.3208/sandf.41.
- Tapias M, Alonso EE, Gili J (2015) A particle model for rockfill behaviour. Géotechnique 65(11):975–994. https://doi.org/10. 1680/geot.14.P.170
- Ting JM, Corkum BT, Kauffman CR, Greco C (1989) Discrete numerical model for soil mechanics. ASCE J Geotech Engng 115(3):379–398
- 68. Tran TH, Vénier R, Cambou B (2009) Discrete modelling of rock-ageing in rockfill dams. Comput Geotech 36(1–2):264–275
- Wang J, Xia Z (2021) DEM study of creep and stress relaxation behaviors of dense sand. Comput Geotech 134:104142. https:// doi.org/10.1016/j.compgeo.2021.104142
- Wang Y-H, Xu D, Tsui KY (2008) Discrete Element Modeling of Contact Creep and Aging in Sand. J Geotech Geoenviron Eng 134(9):1407–1411. https://doi.org/10.1061/(ASCE)1090-0241(2008)134:9(1407)
- Xu M, Hong J, Song E (2018) DEM study on the macro- and micro-responses of granular materials subjected to creep and stress relaxation. Comput Geotech 102:111–124. https://doi.org/ 10.1016/j.compgeo.2018.06.009
- Yang D, Chu X (2024) Influence of particle shape on creep and stress relaxation behaviors of granular materials based on DEM. Comput Geotech 166:105941
- Zhang YD, Buscarnera G (2017) A rate-dependent breakage model based on the kinetics of crack growth at the grain scale. Géotechnique 67(11):953–967. https://doi.org/10.1680/jgeot.16. p.181
- Zhang N, Ciantia MO, Arroyo M, Gens A (2021) A contact model for rough crushable sand. Soils Found 61(3):798–814. https://doi.org/10.1016/j.sandf.2021.03.002



75. Zhang C, Yang ZX, Nguyen GD, Jardine RJ, Einav I (2014) Theoretical breakage mechanics and experimental assessment of stresses surrounding piles penetrating into dense silica sand. Géotechnique Lett 4:11–16 **Publisher's Note** Springer Nature remains neutral with regard to jurisdictional claims in published maps and institutional affiliations.